Supporting Information

Au_{25} Nanocluster/MoS_2 vdWaals Heterojunction Phototransistor for Chromamorphic Visual-afterimage Emulation

Zhuohui Huang[a,b,1], Chuanjia Tong[a,1], Yanbo Zhao[a], Leyong Jiang[c], Lianwen Deng[a], Xiaohui Gao[a,*], Jun He[a,*], and Jie Jiang[a,b,*]

[a]Hunan Key Laboratory of Nanophotonics and Devices, School of Physics, Central South University, Changsha, Hunan 410083, China

[b]State Key Laboratory of Precision Manufacturing for Extreme Service Performance, College of Mechanical and Electrical Engineering, Central South University, Changsha, Hunan 410083, China

[c]School of Physics and Electronics, Hunan Normal University, Changsha, Hunan 410081, China

E-mail: xiaohuigao@csu.edu.cn; junhe@csu.edu.cn; jiangjie@csu.edu.cn

Note S1. The analysis of the electrical properties of Au_{25} NCs/MoS_2 heterojunction transistor.

To reveal the use of Au_{25} NCs in heterojunction transistors, we compared the transfer curves of pure MoS_2 and Au_{25} NCs/MoS_2 heterojunction transistors. As shown in Figures S3 and S4, the transfer curves are depicted for a forward sweep from -20V to 20V and a reverse sweep from 20V to -20V at a constant V_{DS} of 0.1V. The transfer curves of the heterojunction transistor are significantly shifted in the positive direction along the y-axis compared to the pure MoS_2 transistor, which is attributed to the N-doping from Au_{25} NCs [1]. The field-effect mobility (μ) can be extracted from the following equation (1):

$$\mu = \frac{L}{W \cdot C_i \cdot V_{DS}} \cdot \frac{dI_{DS}}{dV_G} \quad (1)$$

where $L = 8\ \mu m$ is the channel length, $W = 4\ \mu m$ is the channel width, and $C_i \approx 1.2\times10^{-8}$ F/cm^2 is the capacitance with 300 nm SiO_2 thickness. From the linear coordinates of the transfer curves, the maximum slopes of the curves can be obtained for forward and backward sweeps, respectively. The mobility of the pure MoS_2 transistor is thus calculated to be 2.67 $cm^2 \cdot V^{-1} \cdot s^{-1}$ for a forward sweep and 13.3 $cm^2 \cdot V^{-1} \cdot s^{-1}$ for a backward sweep. In comparison, the mobility of the Au_{25} NCs/MoS_2 heterojunction transistor was calculated to be 21.7 $cm^2 \cdot V^{-1} \cdot s^{-1}$ for a forward sweep and 34 $cm^2 \cdot V^{-1} \cdot s^{-1}$ for a backward sweep, all have improved considerably.

In addition, we fabricated a new Au_{25} NCs/MoS_2 heterojunction device to study the transfer characteristics. The stability of the transfer characteristics of our heterojunction transistors after storage in air is reasonable and acceptable, as shown in Figure S6. It can be observed from the figure that the Au_{25} NCs/MoS_2 heterojunction transistor not only maintains the same current level for 30 consecutive tests but also the transfer and output currents after storage in air (3 days of consecutive measurements) maintain almost the same current level.

Note S2. The analysis of improved optoelectronic properties of Au_{25} NCs/MoS_2 heterojunction transistor.

To investigate the effect of Au_{25} NCs in heterojunction transistors on the optoelectronic properties, we compare the transfer curves of pure MoS_2 transistors at different wavelengths with those of Au_{25} NCs/MoS_2 heterojunction transistors, as shown in Figure S7. It can be seen

that without Au_{25} NCs, the pure MoS_2 transistor exhibits higher On-state currents for short wavelengths (450 nm). This is consistent with previous reports and also confirms that the higher ON state currents of the Au_{25} NCs/MoS_2 heterojunction transistor under 520 nm illumination are due to the matching of the Au_{25} NCs/MoS_2 heterojunction with the 520 nm photon energy. In addition, we also compared the output curves of pure MoS_2 and Au_{25} NCs/MoS_2 heterojunction transistors at different wavelengths, as shown in Figure S8. Apparently, the pure MoS_2 transistor exhibits a low optical response to each wavelength, which quickly saturates with increasing V_{DS}. In contrast, after the incorporation of Au_{25} NCs as an efficient light-absorbing layer, the Au_{25} NCs/MoS_2 heterojunction transistor exhibits a high photoresponse and maintains a linearly increasing photocurrent trend even in the high V_{DS} region.

Note S3. Fitting analysis of the memory factor in Figure 5f (main text)

As shown in Figure 5f (main text), it is clearly seen that the λ can be well-fitted with a single exponential function as the following equation:

$$\lambda = \lambda_0 + C_0 e^{\frac{-f}{f_0}} \quad (2)$$

where λ_0 and C_0 denote two different memory constants, respectively. f_0 denotes the characteristic frequency constant. Furthermore, the fitting results of these parameters are summarized in Table S2.

Note S4. The process of calculating the band structure of Au_{25} NCs/MoS_2 heterojunction with DFT.

Geometry optimization and electronic structure calculations were performed using density functional theory (DFT), as implemented in the Vienna ab Initio Simulation Package (VASP) [2]. The projected augmented wave (PAW) method was adopted to treat interactions of valence electrons with ion cores. The Perdew–Burke–Ernzerhof (PBE) functional was used to describe electron exchange–correlation interactions. The van der Waals (vdW) interactions were considered [3–5]. A plane wave energy cutoff of 500 eV was set, while geometry optimization was terminated when the ion forces fell below 0.01 eV/Å and the total energy

change fell below 10^{-5} eV. The hexagonal bulk 2H-MoS_2 was selected and one single k-point was used for the whole system.

Note S5. Some key parameters of photodetectors.

Table 1. External quantum efficiency and photoluminescence at three wavelengths (the light intensity is fixed at 50 mW)

λ (nm)	R (A/W)	EQE (%)
450	355.06	84.73
520	473.50	112.99
635	129.56	25.32

Supplementary Figures

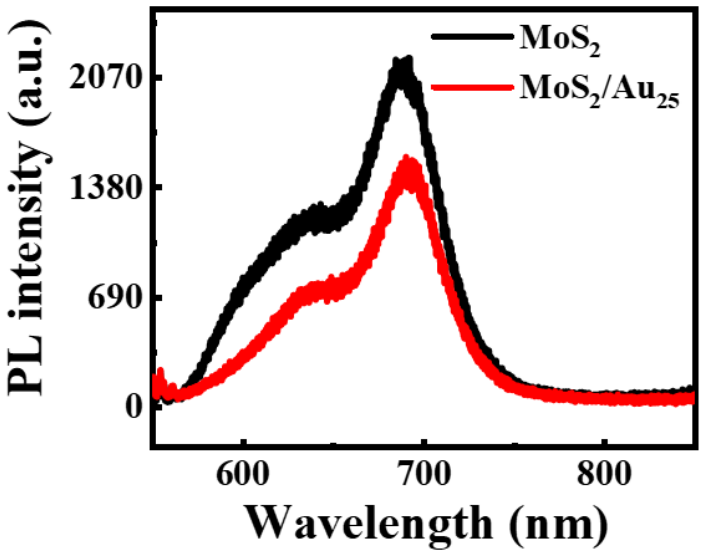

Figure S1. The PL spectra of MoS_2 and Au_{25} NCs/MoS_2.

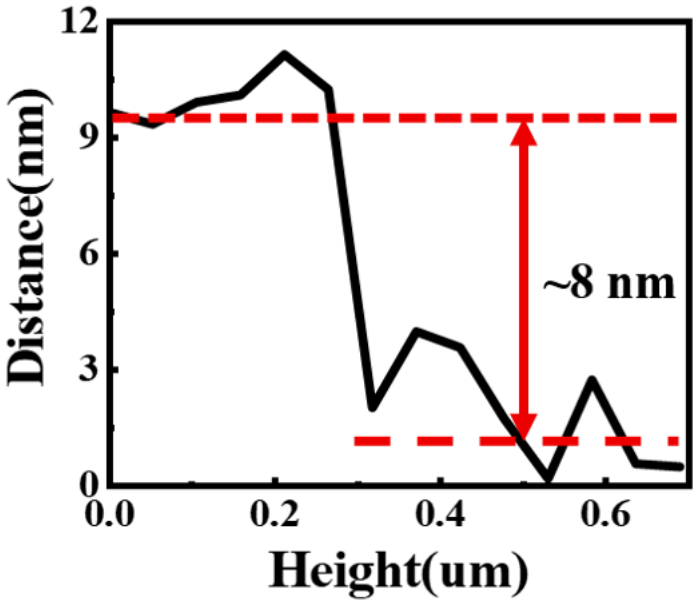

Figure S2. The thickness of MoS_2 (8 nm) is measured through AFM measurement.

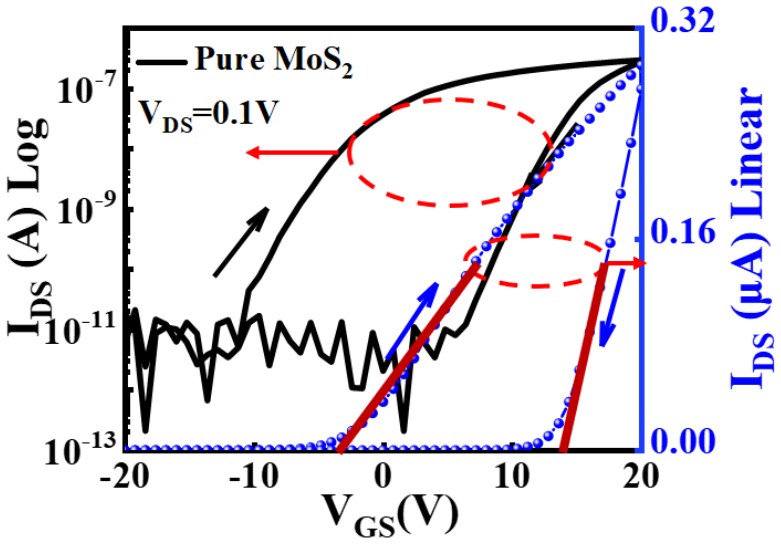

Figure S3. The transfer curve of MoS_2 transistor without Au_{25} NCs at V_{DS}=0.1V. The black line represents the logarithmic scale and the dotted blue line shows the linear scale.

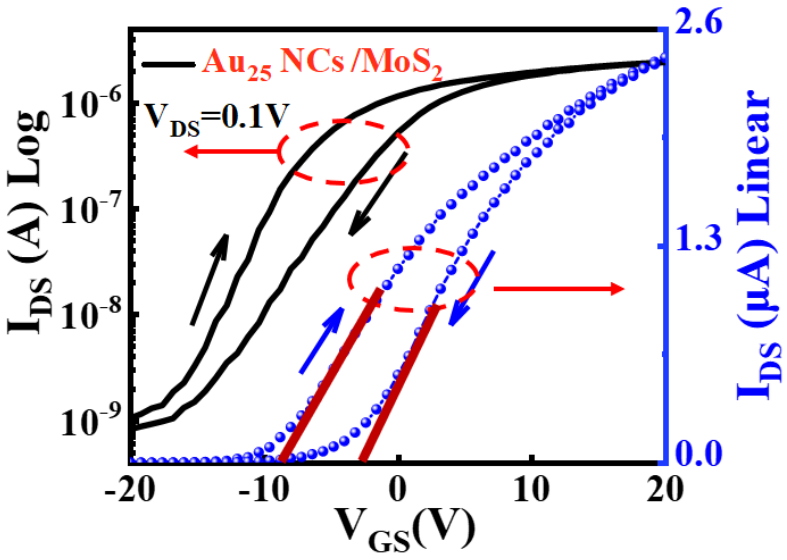

Figure S4. The transfer curve of an Au_{25} NCs/MoS_2 mixed-dimensional heterojunction transistor with a fixed V_{DS} of 0.1 V. The black line represents the logarithmic scale and the dotted blue line shows the linear scale.

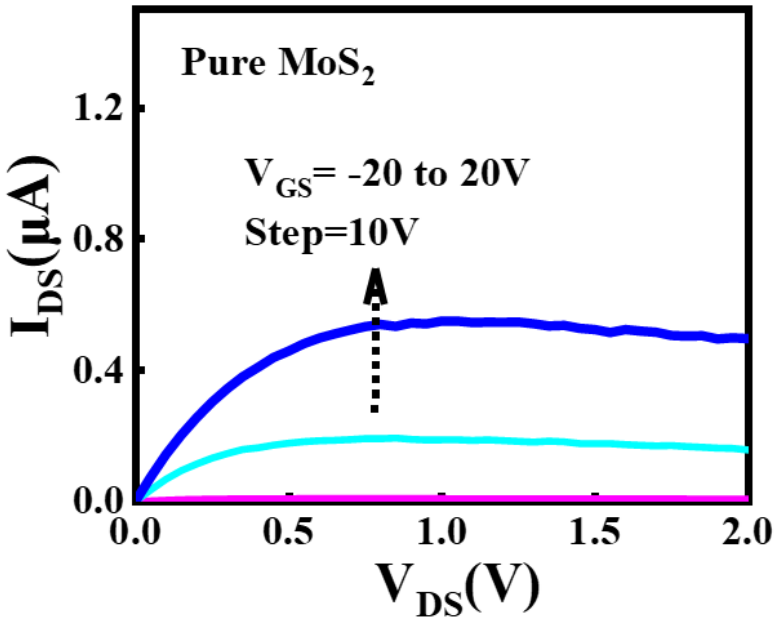

Figure S5. The output curves of pure MoS_2 transistor.

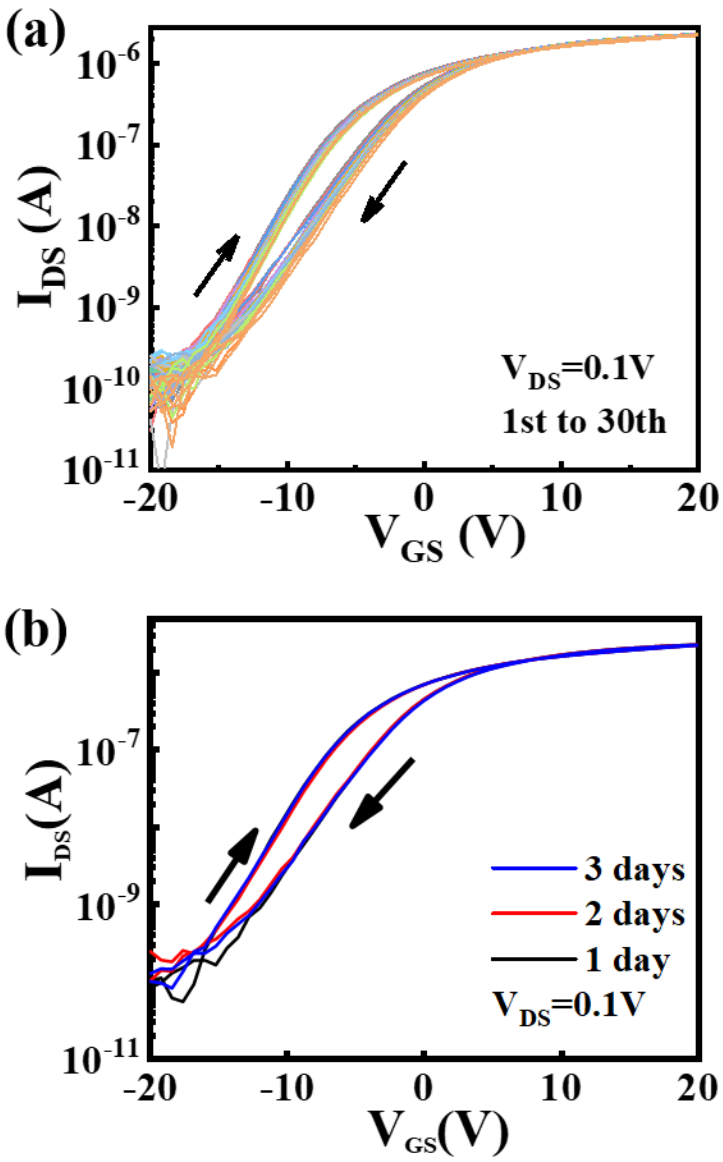

Figure S6. The stability of the transfer characteristics of our Au_{25} NCs/MoS_2 heterojunction devices (a) after 30 consecutive measurements and (b) storage in air (consecutive measurements for 3 days).

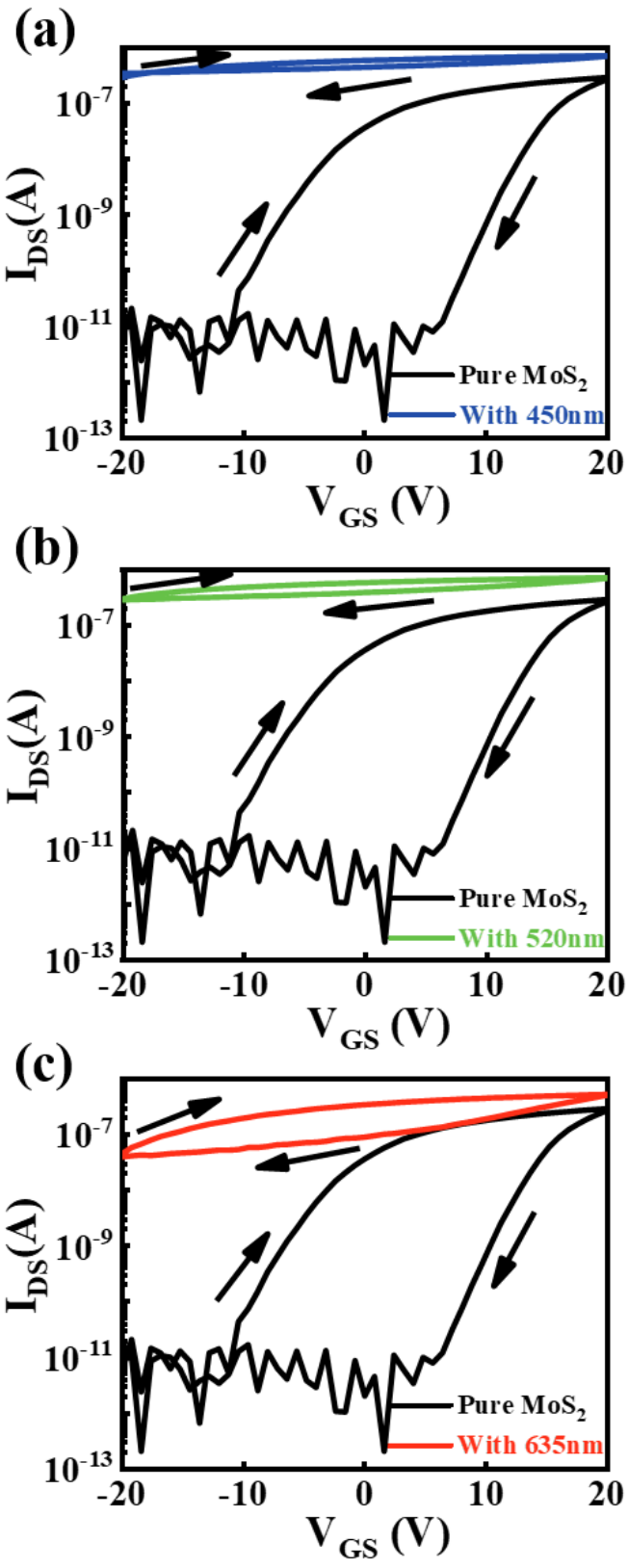

Figure S7. The transfer curves of MoS_2 transistor under different wavelengths of light, respectively: (a) 450 nm (b) 520 nm (c) 635 nm. V_{DS} is fixed at 0.1 V and the light intensity is 50 mW cm^{-2}.

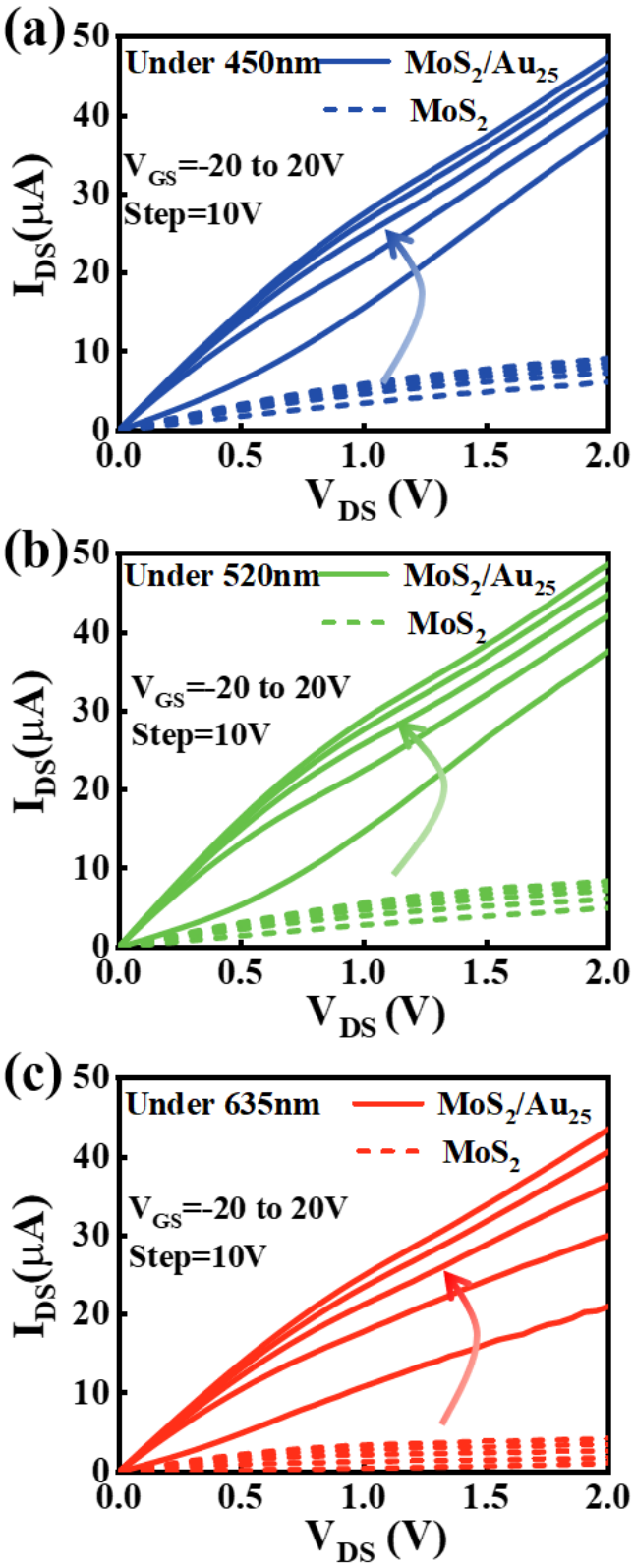

Figure S8. The comparative output curves of MoS_2 and Au_{25} NCs/MoS_2 heterojunction transistor at different wavelengths of light at (a) 450 nm (b) 520 nm (c) 635 nm.

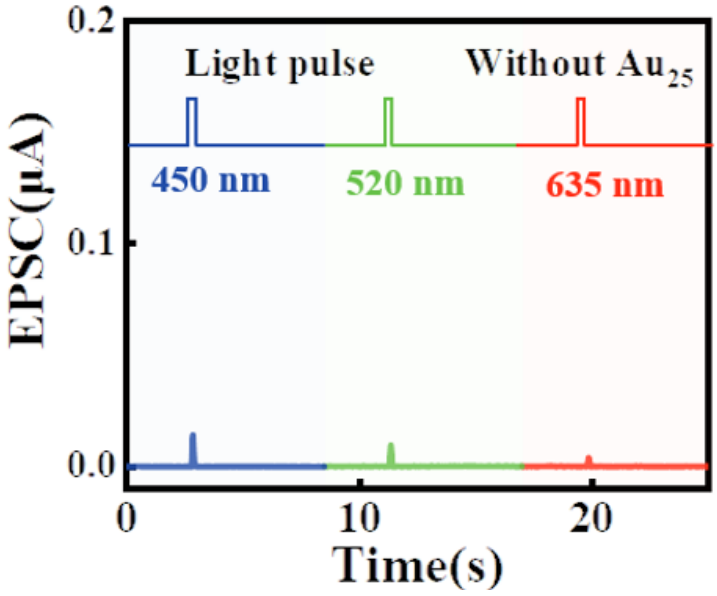

Figure S9. The EPSC response of pure MoS_2 transistor without Au_{25} NCs under different wavelengths of light. Δt=10ms, light intensity fixed at 50 mW cm^{-2}.

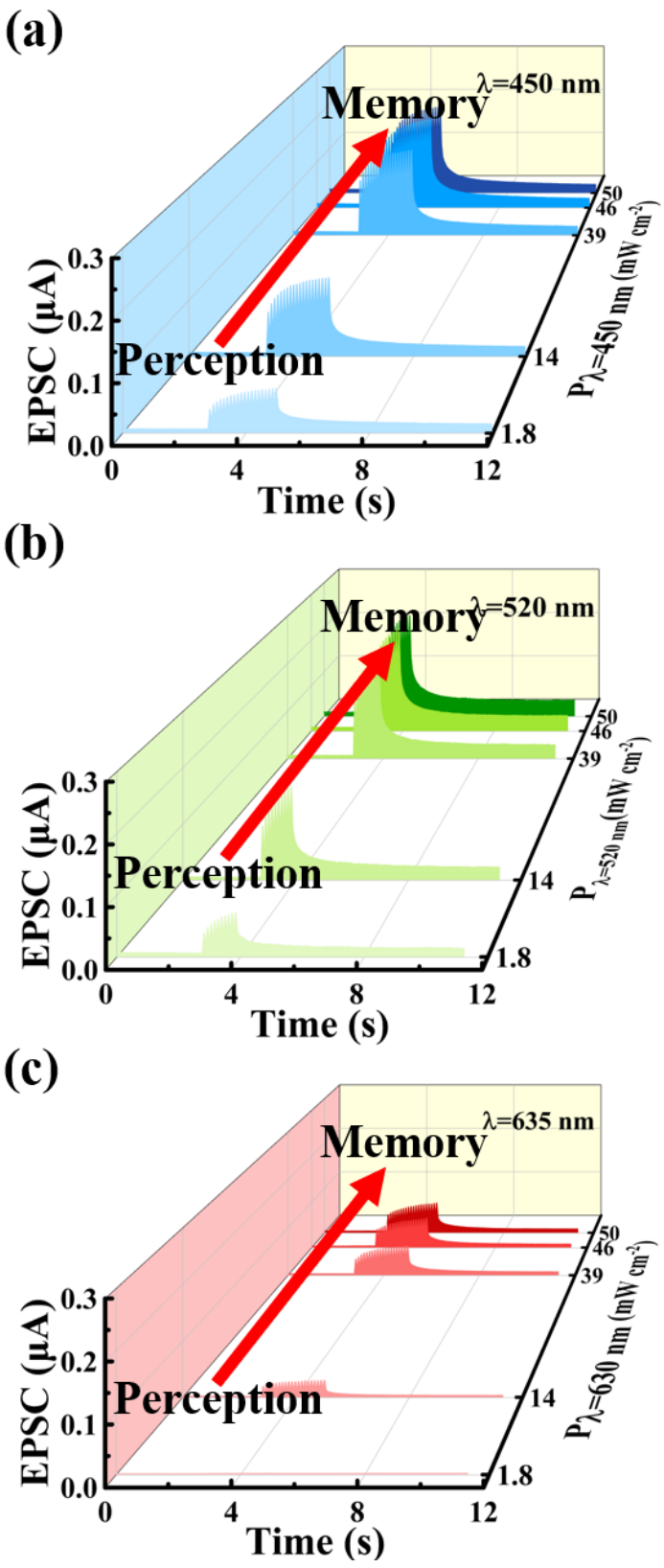

Figure S10. The transition from STM to LTM was induced by increasing the light intensity of optical spikes of different wavelengths in the Au_{25} NCs/MoS_2 heterojunction transistor: (a) 450 nm, (b) 520 nm, (c) 635 nm.

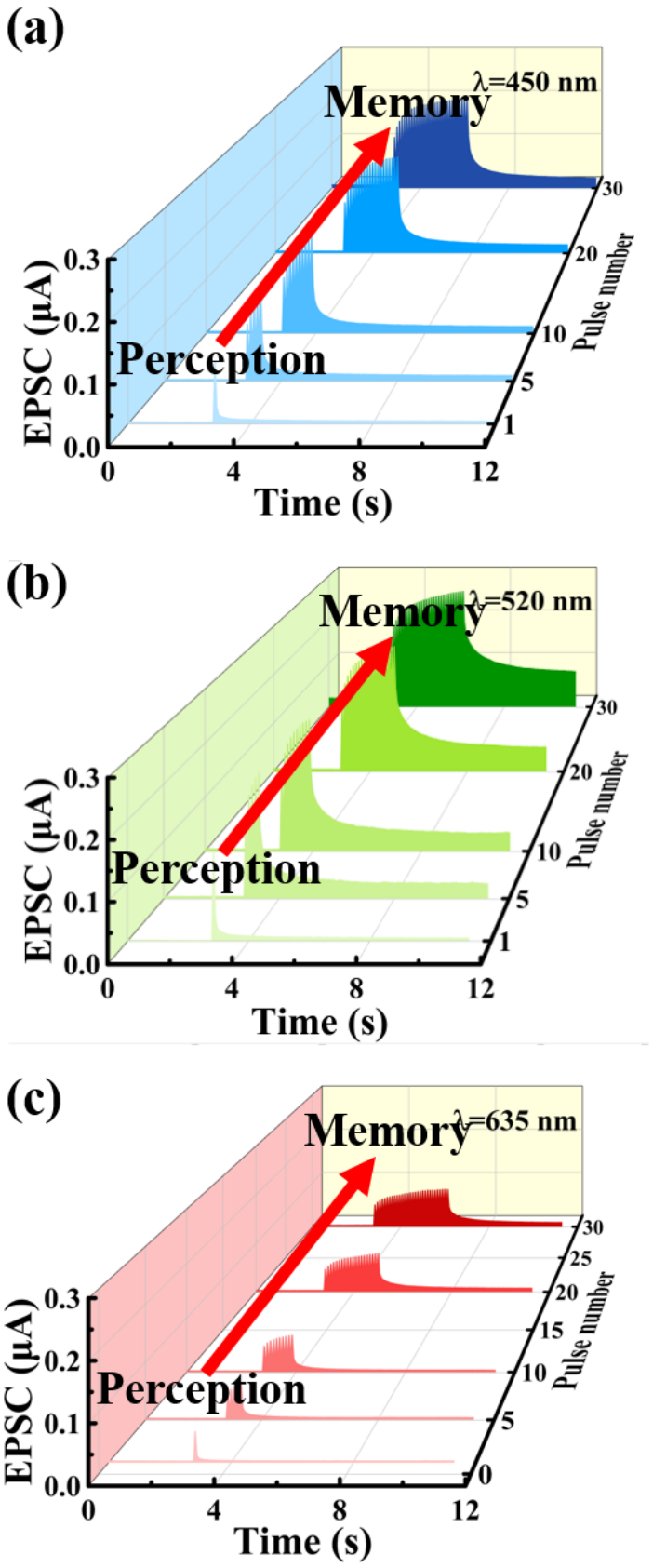

Figure S11. The transition from STM to LTM was induced by increasing the numbers of optical spikes of different wavelengths in the Au_{25} NCs/MoS_2 heterojunction transistor: (a) 450 nm, (b) 520 nm, (c) 635 nm.

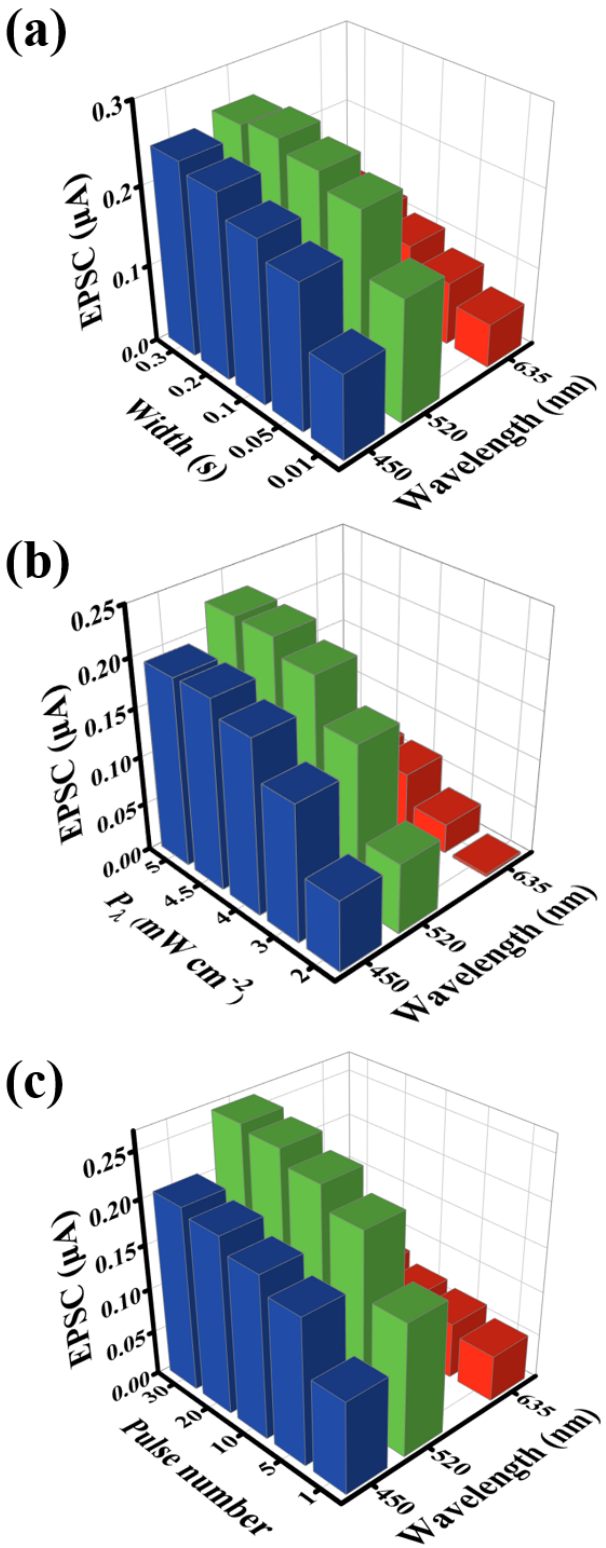

Figure S12. The change values of EPSCs are induced by various (a) widths, (b) light intensities, and (c) numbers of optical spikes with different wavelengths of 450 nm, 520 nm, and 635 nm, respectively.

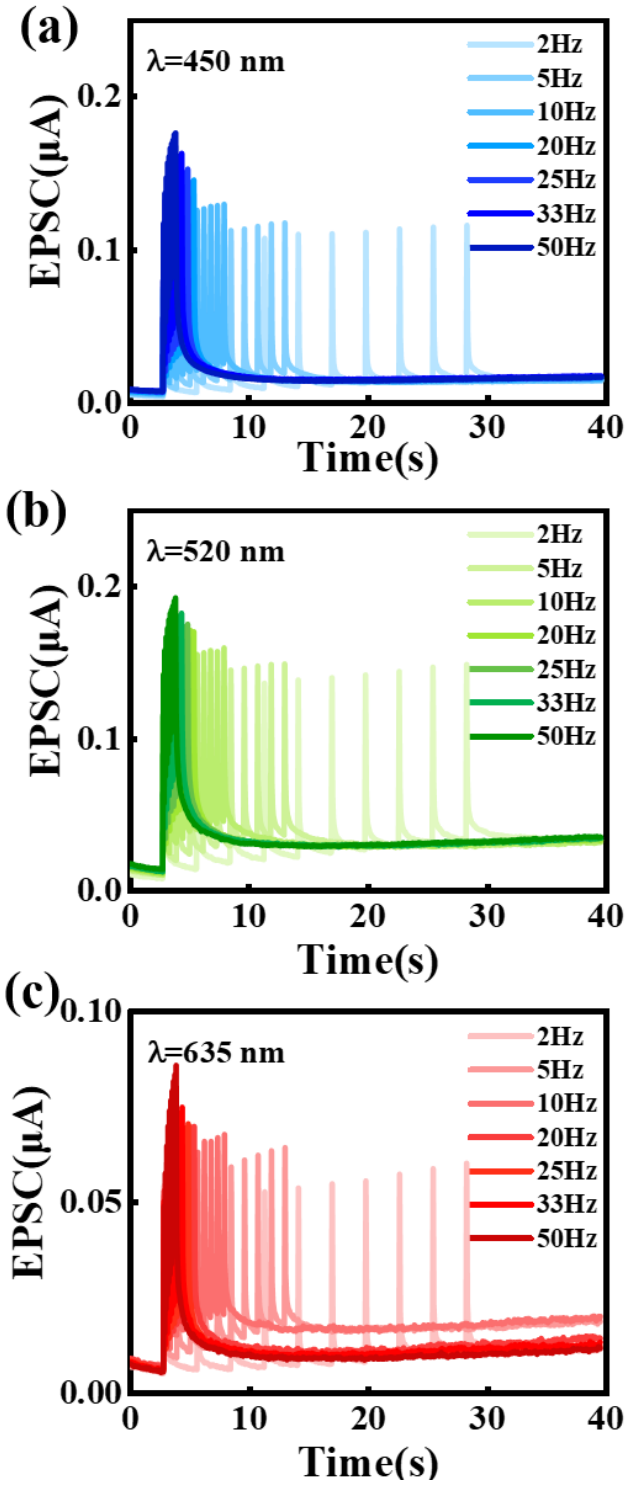

Figure S13. The EPSC responses induced by frequency-dependent changes of 10 optical spikes at different wavelengths: (a) 450 nm, (b) 520 nm, (c) 635 nm.

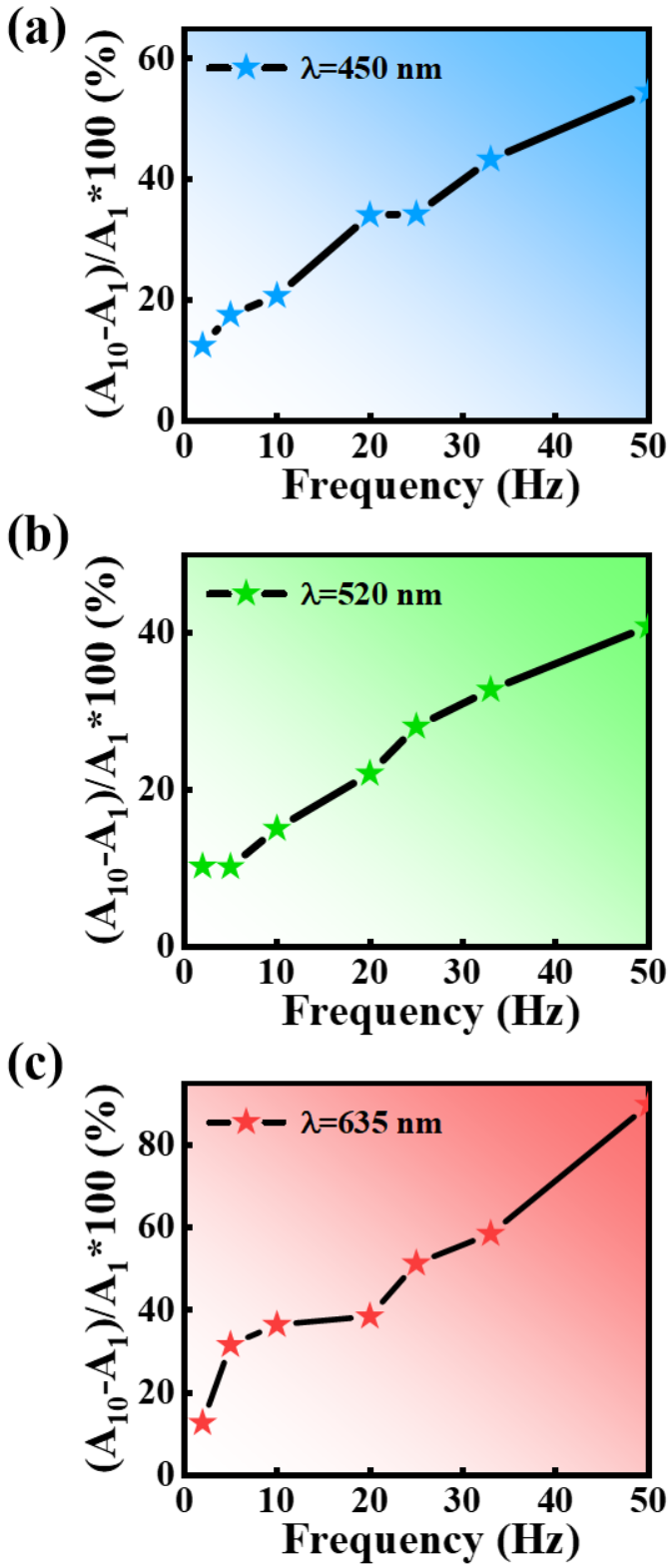

Figure S14. The EPSC gain of the high-pass filter ($(A_{10}-A_1)/A_1$ 100%) as a function of different frequencies. Ten consecutive optical pulses at different wavelengths: (a) 450 nm, (b) 520 nm, (c) 635 nm.

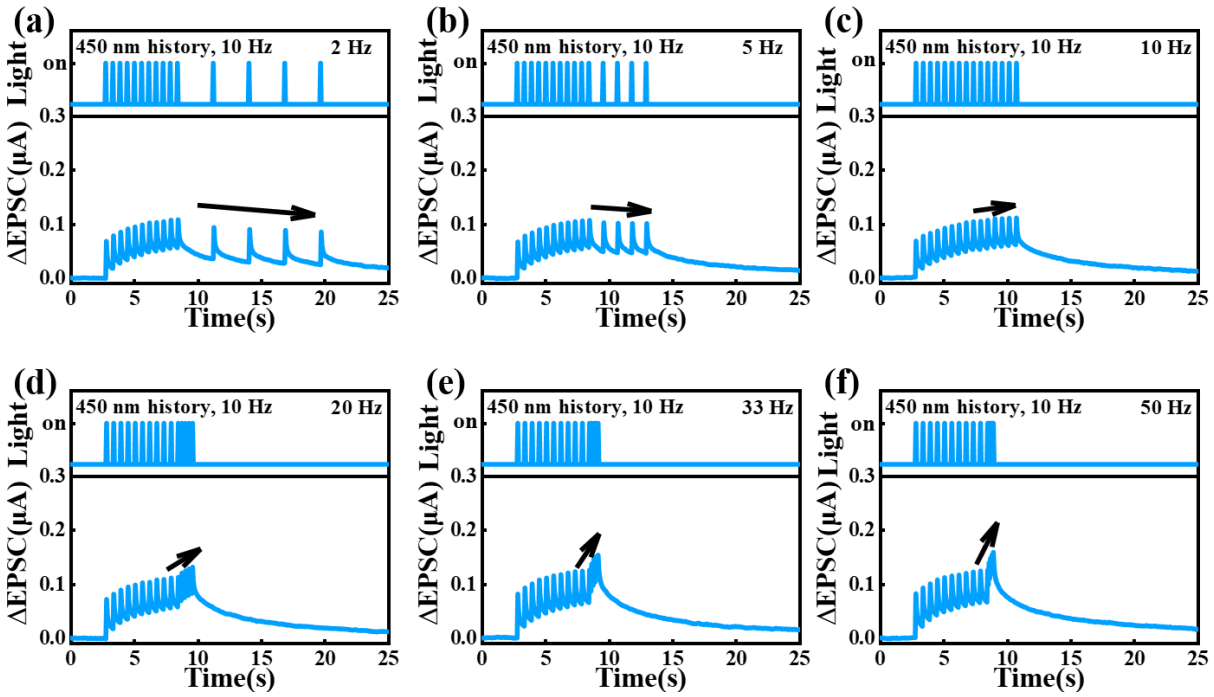

Figure S15. The photocurrent response of a 450 nm optical spike at different frequencies under fixed a $f_{history}$ of 10 Hz.

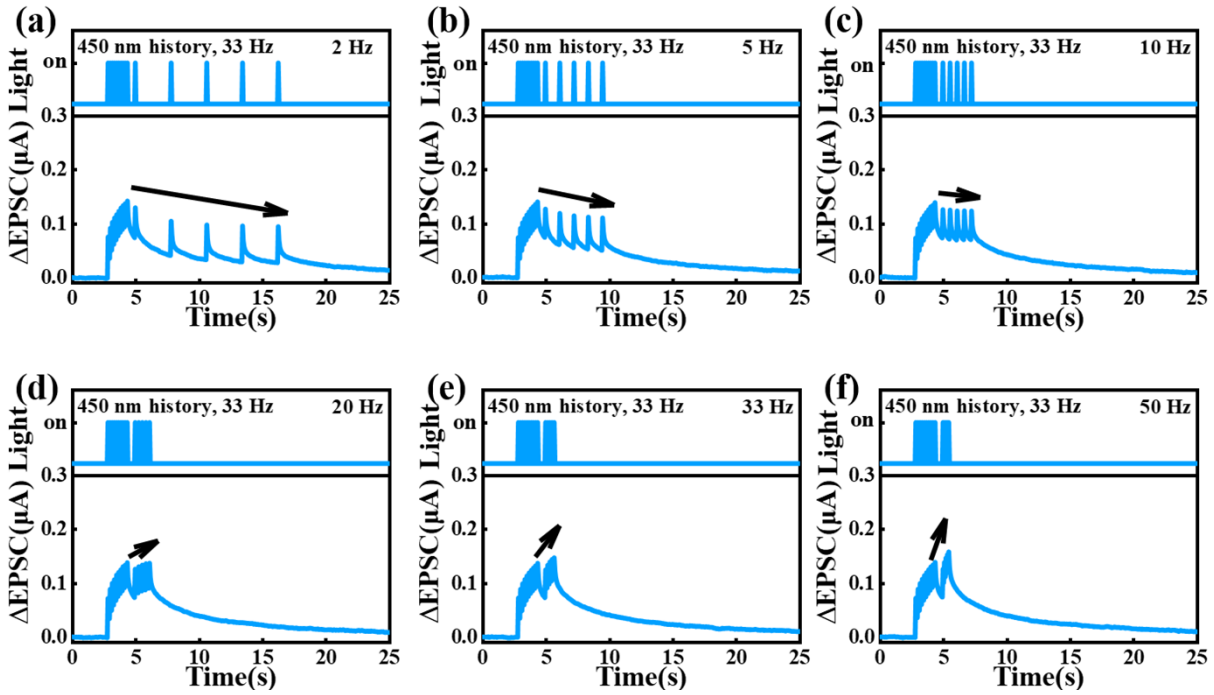

Figure S16. The photocurrent response of a 450 nm optical spike at different frequencies of 2 Hz under a fixed $f_{history}$ of 33 Hz.

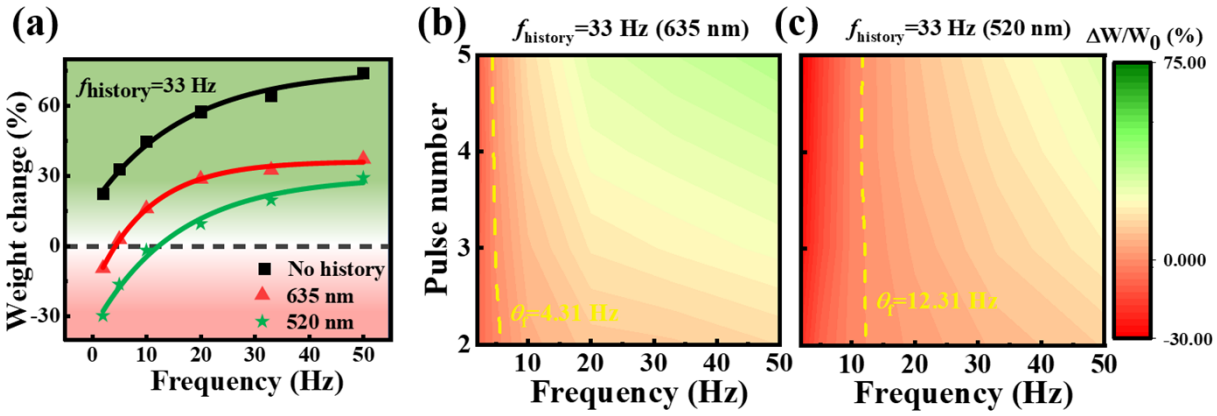

Figure S17. (a) Color-dependent sliding threshold effects at a fixed historical frequency of 33 Hz. The contour plots of ΔW to check the slip of θ_f with the number and frequency of pulses. At different historical optical pulses: (a) 635 nm at a frequency of 33 Hz, and (b) 520 nm at a frequency of 33 Hz.

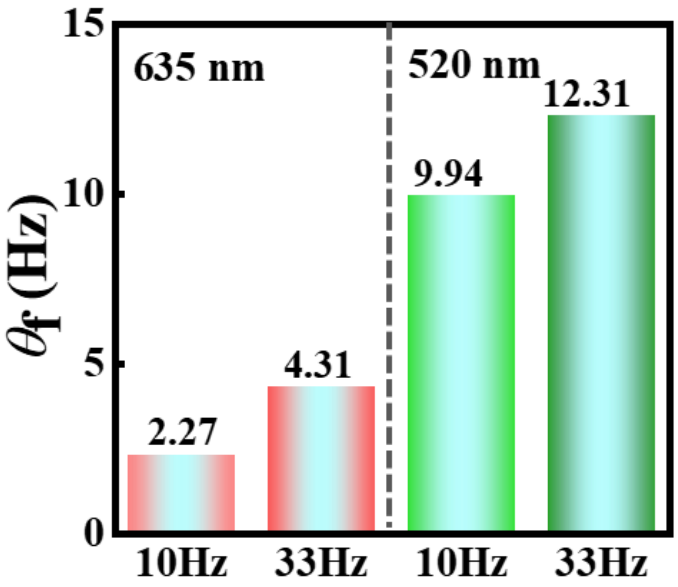

Figure S18. Extracting θ_f as a function of pulse width for different color history.

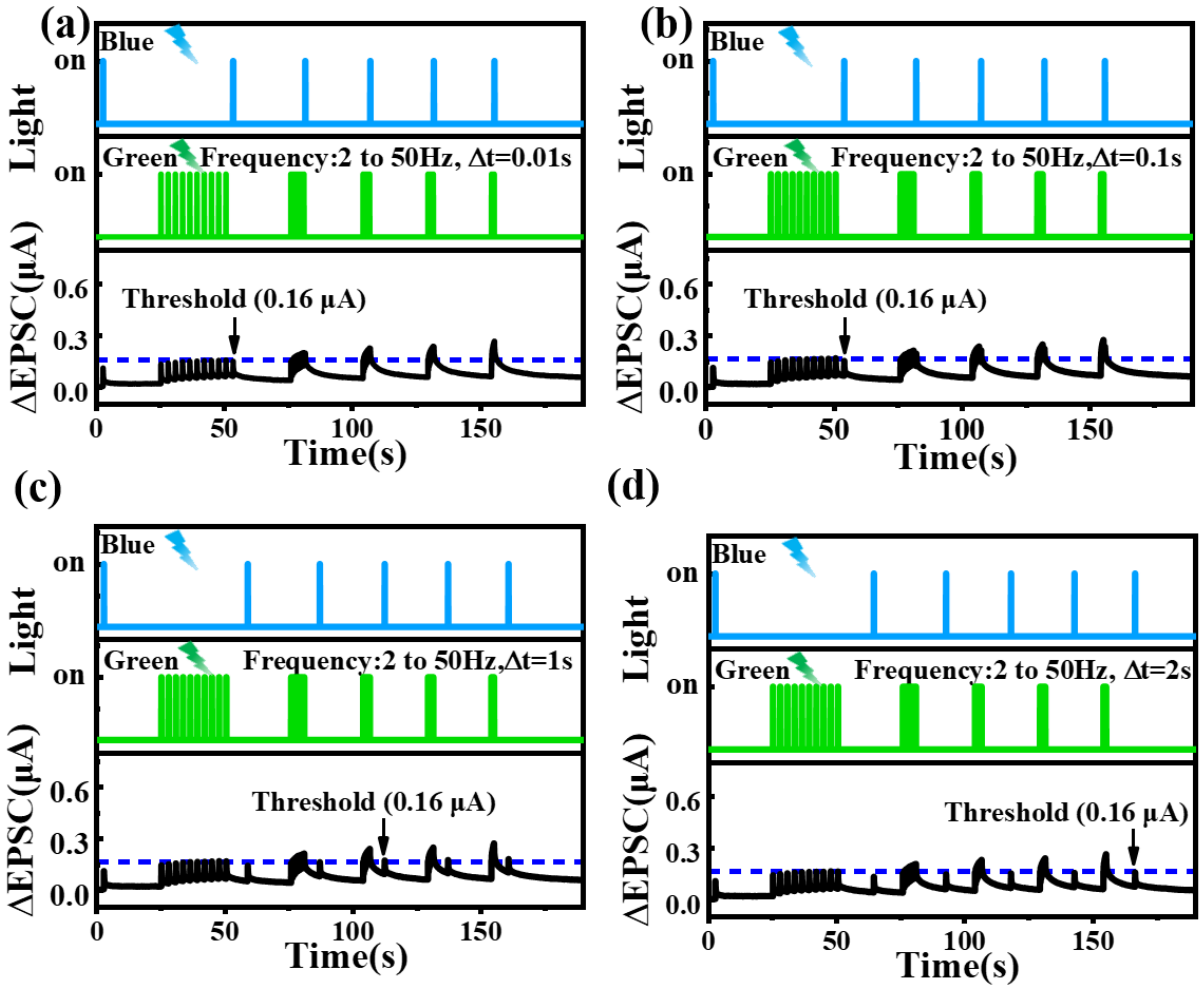

Figure S19. ΔEPSCs are triggered by pulses of different frequencies to emulate visual impressions from fragmentary memory to gradual clarity. Fixed at different interval times (Δ*t*): (a) Δ*t*=0.01s, (b) Δ*t*=0.1 s, (c) Δ*t*=1s, (d) Δ*t*=2 s..

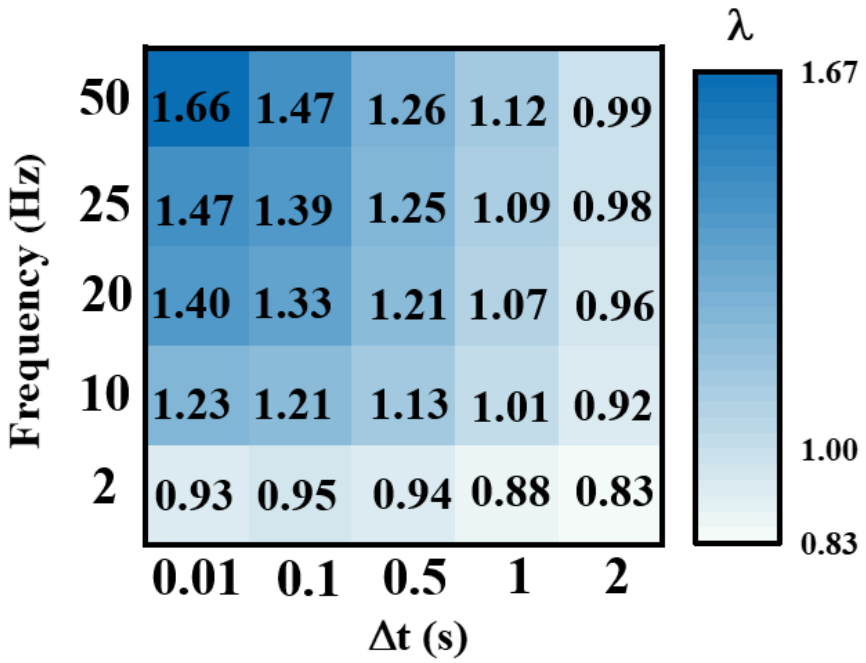

Figure S20. The detailed values of λ are shown with different Δt.

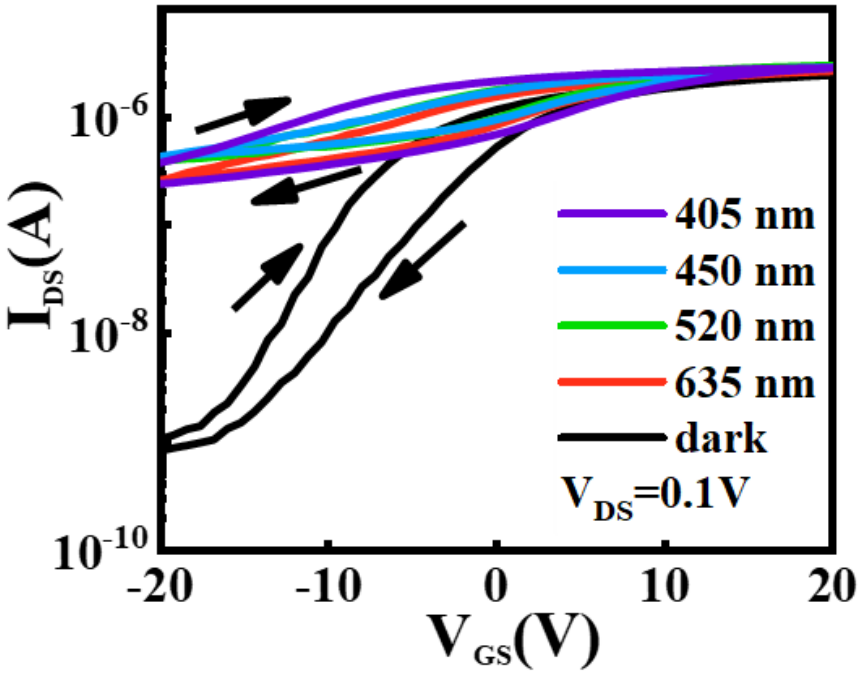

Figure S21. The transfer curves of Au_{25} NCs/MoS_2 heterojunction transistors under four different wavelengths of light.

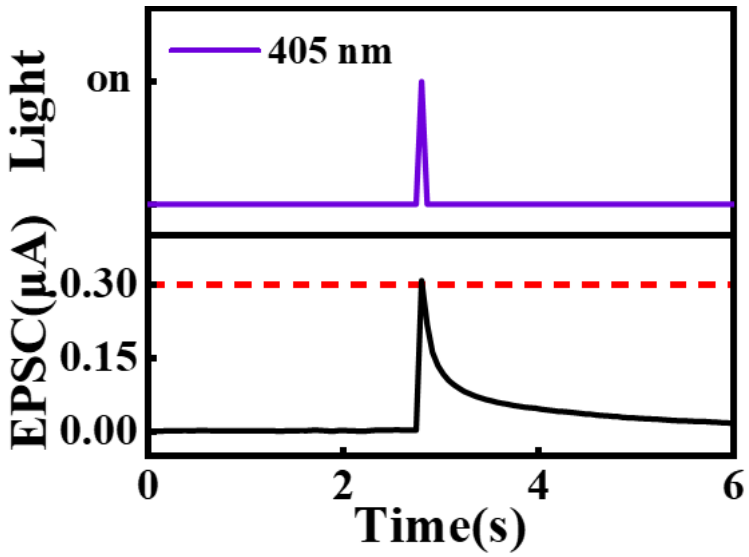

Figure S22. The EPSC response to 405 nm light stimulus. The pulse duration was 10 ms. The light sources used in the above figures were all 50 mW cm^{-2}.

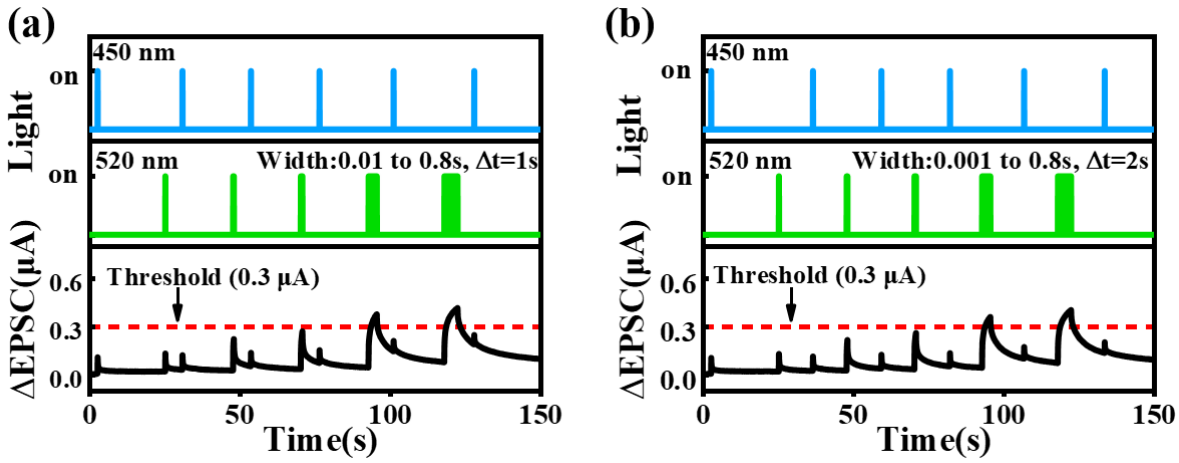

Figure S23. ΔEPSC values triggered by blue light stimulus after green light induction for five different gaze durations to emulate the visual afterimage from a blue afterimage to an induced violet negative afterimage. Fixed at different interval times (Δ*t*): (a) Δ*t*=1 s, (b) Δ*t*=2 s.

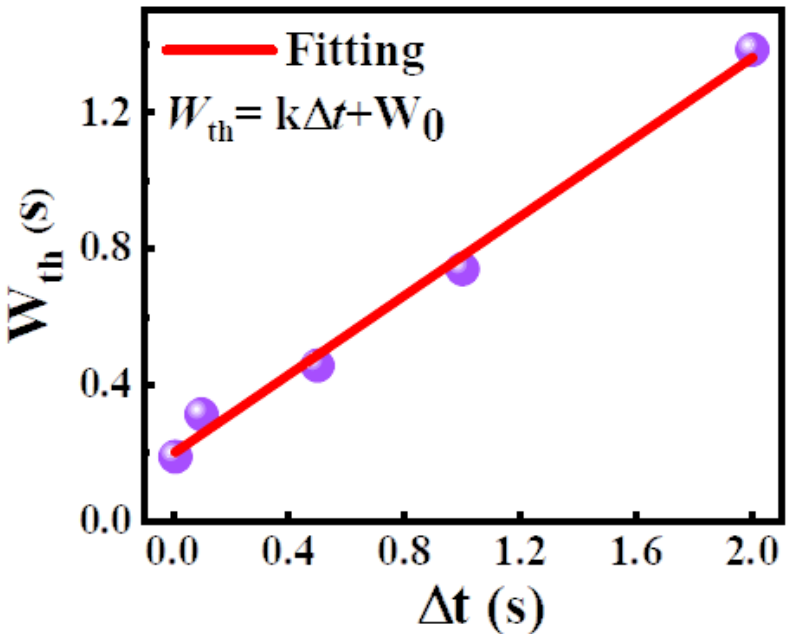

Figure S24. The derived W_{th} as a function of interval times. The red line represents the linear fitting of the experimental data.

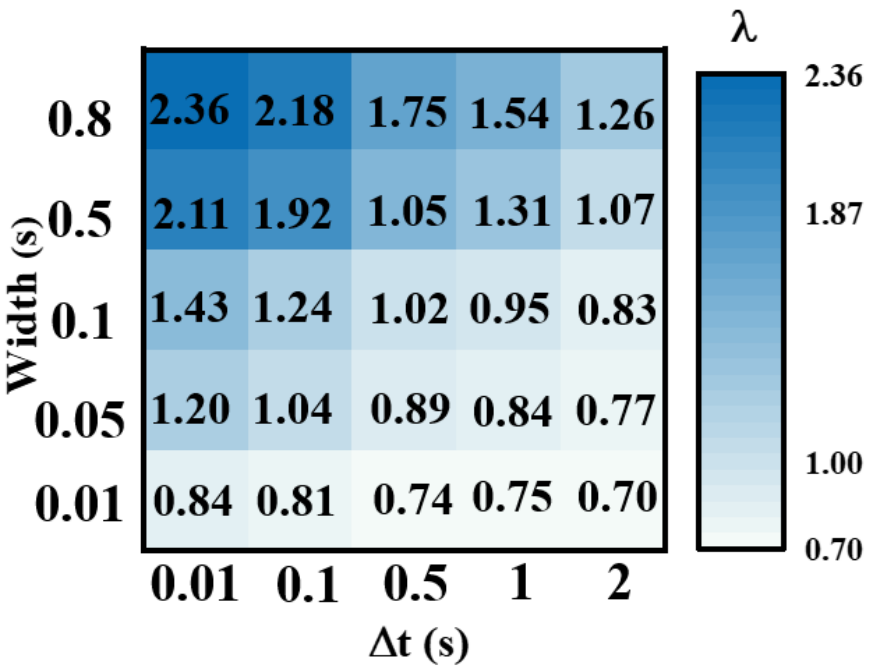

Figure S25. The detailed values of λ are shown with different Δt.

Supplementary Tables

Table S1. The fitting results are summarized in Figure 3d in the main text.

λ (nm)	τ_1(s)	τ_2(s)
450	0.013	0.150
520	0.014	0.165
635	0.128	0.129

Table S2. The summarized table of the fitting results (λ_0 , C_0, and f_0) for memory factor

	Interval time (s)				
	0.01	0.1	0.5	1	2
λ_0	1.73	1.46	1.26	1.12	1.0
C_0	-0.88	-0.60	-0.40	-0.29	-0.20
f_0	20.00	11.95	9.16	10.94	11.55

Supplementary References

(1) Yan, F.; Liao, C.-K.; Mahmoud, M. A.; Bach, S. B. Electron Doping of Semiconducting MoS_2 Nanosheets by Silver or Gold Nanoclusters. *Langmuir* **2022**, *38* (14), 4378–4388.

(2) Kresse, G.; Furthmüller, J. Efficient Iterative Schemes for Ab Initio Total-Energy Calculations Using a Plane-Wave Basis Set. *Phys. Rev. B* **1996**, *54* (16), 11169–11186.

(3) Blöchl, P. E. Projector Augmented-Wave Method. *Phys Rev B Condens Matter* **1994**, *50* (24), 17953–17979.

(4) Perdew, J. P.; Burke, K.; Ernzerhof, M. Generalized Gradient Approximation Made Simple. *Phys. Rev. Lett.* **1996**, *77* (18), 3865–3868.

(5) Grimme, S.; Antony, J.; Ehrlich, S.; Krieg, H. A Consistent and Accurate Ab Initio Parametrization of Density Functional Dispersion Correction (DFT-D) for the 94 Elements H-Pu. *The Journal of Chemical Physics* **2010**, *132* (15), 154104.